Dissociative electron attachment to 5-bromo-uracil: non-adiabatic dynamics on complex-valued potential energy surfaces†

Lucas M. Cornetta, *[a] Todd J. Martinez [bc] and Marcio T. do N. Varella [d]

Electron induced dissociation reactions are relevant to many fields, ranging from prebiotic chemistry to cancer treatments. However, the simulation of dissociation electron attachment (DEA) dynamics is very challenging because the auto-ionization widths of the transient negative ions must be accounted for. We propose an adaptation of the *ab initio* multiple spawning (AIMS) method for complex-valued potential energy surfaces, along the lines of recent developments based on surface hopping dynamics. Our approach combines models for the energy dependence of the auto-ionization widths, obtained from scattering calculations, with survival probabilities computed for the trajectory basis functions employed in the AIMS dynamics. The method is applied to simulate the DEA dynamics of 5-bromo-uracil in full dimensionality, *i.e.*, taking all the vibrational modes into consideration. The propagation starts on the π_2^* resonance state and describes the formation of Br^- anions mediated by non-adiabatic couplings. The potential energies, gradients and non-adiabatic couplings were computed with the fractional-occupancy molecular orbital complete-active-space configuration-interaction method, and the calculated DEA cross section are consistent with the observed DEA intensities.

Received 11th December 2021,
Accepted 25th February 2022

DOI: 10.1039/d1cp05663h

1 Introduction

Electron induced dissociation reactions[1] are relevant to many scientific and technological fields, including plasma processing,[2,3] astrophysics,[4] atmospheric sciences,[5,6] materials[7,8] and nano[9–11] sciences, prebiotic chemistry,[12–14] radiation damage to biomolecules,[15–21] and chemo-radiation cancer treatments.[22–26] In some aspects, those dissociative electron attachment (DEA) processes are similar to photochemical and photophysical phenomena. The vibration dynamics are initiated by sudden changes in the potential energy surfaces (PESs), induced by either photon absorption or electron attachment (EA), and non-adiabatic couplings often play a prominent role in the reaction pathways. The electronic states are also quasi-stationary, since the excited states of neutral molecules and the anion states formed by EA can decay, respectively, by spontaneous emission and autoionization. Nevertheless, photoemission can be safely neglected in ultrafast phenomena, in view of the large time scales compared to those for vibrational relaxation, internal conversion and dissociation, while electron detachment typically takes place on the femtosecond timescale.

The inherently short-lived transient negative ions (TNIs) pose a challenge to theory, since conventional electronic structure methods, based on spatially localized wave functions, cannot account for the coupling to the continuum of autoionization states. To incorporate the electron detachment widths, one usually resorts to scattering[27] or modified quantum chemistry methods,[28] which are significantly more computationally intensive than conventional electronic structure theory (assuming a similar description of electronic correlation). This is the main reason why the gap between theory and experiment is much more significant in DEA studies than in photodynamics. Formally the TNI potentials depend non-locally on the electronic energy and vibrational coordinates.[29] The inclusion of these non-local effects, which can be relevant for broad resonances and near-threshold phenomena, is restricted to diatomics or pseudo-diatomic models.[30–33] Also, most of the DEA studies employ the local approximation[29] to build complex PESs, whose imaginary parts account for autoionization. Even in this case the computations are restricted to small molecules or reduced dimensionality models with up to three vibrational

[a] *Instituto de Física Gleb Wataghin, Universidade Estadual de Campinas, Rua Sérgio Buarque de Holanda, 777 - Cidade Universitária, Campinas, São Paulo, Brazil. E-mail: lucascor@unicamp.br*
[b] *Department of Chemistry and PULSE Institute, Stanford University, Stanford, California 94305, USA*
[c] *SLAC National Accelerator Laboratory, Menlo Park, CA 94025, USA*
[d] *Instituto de Física, Universidade de São Paulo, Rua do Matão 1371, 05508-090, São Paulo, São Paulo, Brazil*

† Electronic supplementary information (ESI) available. See DOI: 10.1039/d1cp05663h

coordinates.[34–40] Thus, important dynamical aspects of DEA processes in small and medium sized molecules are not fully understood.

When dealing with small to medium sized molecules, DEA can be direct or indirect, depending on whether it requires non-adiabatic coupling between anion states to occur. In the direct DEA mechanism the electron attaches to an antibonding σ* orbital, and the dynamics of the corresponding TNI can be viewed as a competition between autoionization and the fast dissociation. In indirect processes the dissociative state is not directly formed, but instead it is reached *via* internal conversion from another anion state. Particularly for insaturated systems, the formation of a π* resonance followed by a π*/σ* conversion is a relevant mechanism to DNA strand breaks[15] and radiosensitizing activity.[41–43]

We report non-adiabatic DEA simulations for 5-bromo-uracil (BrU) carried out in full dimensionality, *i.e.*, taking all vibrational modes into consideration. BrU is a halo-substituted nucleobase which has been considered as a radiosensitizing drug for cancer treatment.[44,45] The incorporation of BrU into the DNA sequence is known to enhance the electron induced damage to nucleosides and oligonucleotides,[46–48] and its bioactivity is believed to arise, at least in part, from the efficient production of radicals through DEA reactions.[49–51] Our simulations were performed in the doublet spin manifold, and include three vibronically coupled anion states, denoted as π_1^*, π_2^* and σ_{CBr}^* at the vertical attachment geometry[41] (Fig. 1), where the first is a valence bound state and the others are shape resonances. Effects of intersystem crossings were not included in this first application. A connection between resonances an photo-excited states can be made. The π_2^* and σ_{CBr}^* states can be understood as $(\pi_1^* \rightarrow \pi_2^*)$ and $(\pi_1^* \rightarrow \sigma_{CBr}^*)$ single excitations. In view of the relevance of the indirect mechanism, our model considers the bromide (Br^-) elimination channel, with the DEA dynamics starting in the π_2^* anion state. To account for the non-adiabatic TNI dynamics we employ the semiclassical *ab initio* multiple spawning (AIMS) technique,[52] employing a similar approach as that of the recent studies based on surface hopping.[53,54] These methods are representative of on-the-fly mixed-quantum-classical techniques[55,56] which have been broadly applied to photodynamics problems in the last decades. While on-the-fly approaches are the the most efficient way to describe the excited states dynamics in full dimensionality for polyatomic molecules, it would be impractical to perform scattering or modified quantum chemistry computations along the dynamics.[53] We therefore resort to complex PES models based on quantum chemistry techniques, incorporating corrections from scattering calculations. The absolute DEA cross sections are expected to be sensitive to the parametrization, but describing the relative yields of anion fragments for a molecule as large as BrU would be significant in view of the aforementioned difficulties and the amount of data reported in abitrary units. Few theoretical methods have properly addressed the DEA measurements for biomolecules performed in the last two decades, so we hopefully take a step towards bridging this gap.

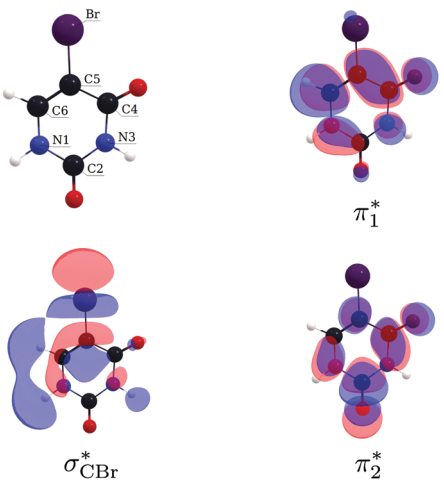

Fig. 1 Equilibrium geometry of the neutral species with the relevant atomic numbering (upper left), and the π_1^*, σ_{CBr}^* and π_2^* orbitals.

2 Theory

In the present semiclassical approach for the TNI dynamics, the physical observables are obtained from nuclear ensemble statistics. The DEA cross sections can be then computed from phase-space integration over the initial conditions.[57,58] The final expression is given by

$$\sigma_{DEA}(E) = \left(\frac{\pi}{E}\right)\frac{1}{N_{IC}}\sum_{j=0}^{N_{IC}} \Gamma(\mathbf{R}_0^j, E) f_\lambda(\mathbf{R}_0^j, E)\wp_j, \qquad (1)$$

where E is the collision energy, N_{IC} is the number of initial conditions $(\mathbf{R}_0^j,\mathbf{P}_0^j)$, $\Gamma(\mathbf{R},E)$ is the autoionization width of the TNI formed by electron attachment (entry width) and $f_\lambda(\mathbf{R}_0^j,E)$ is an empirical broadening function applied to the initial conditions, which is similar to those employed in photoabsorption cross sections computed with the nuclear-ensemble method.[59] The term $\wp_j$ reflects the survival and dissociation probabilities of the j-th initial condition, and will be discussed later in this section.

The AIMS method for non-adiabatic dynamics is well-known, and the details of the theoretical background are available elsewhere.[60–64] The total wave function is given by $|\Psi\rangle = \sum_I \chi_I(\mathbf{R},t)|\psi_I\rangle$, where $|\psi_I\rangle$ are the electronic states and $\chi_I(\mathbf{R},t)$ are nuclear wave functions, which are expanded in a set of time-evolving trajectory basis functions (TBFs). In this work we followed the usual AIMS methodology, so the TBFs are multi-dimensional nuclei-centered frozen Gaussians,[65] with time-dependent phase factors. Each TBF is propagated on its potential energy surface until the trajectory reaches a spawning region, where the non-adiabatic coupling becomes significant. The wave packet might bifurcate (spawn), so the time propagation accounts for the pair of coupled electronic states. In the local approximation,[29] however, resonances are described by complex potential energy surfaces, $E_{res}(\mathbf{R}) - i\Gamma_L(\mathbf{R})/2$, where the

real part (resonance position) is the relative energy of the anion state with respect to the ground state of the neutral molecule. The imaginary part (resonance width) describes the decay to the continuum of autoionization states, $\tau = \hbar/\Gamma_{\mathrm{L}}$, where τ is the lifetime and the subscript L denotes the local approximation. Formally, non-adiabatic transitions between resonance states can involve the continuum ($J \rightarrow$ continuum $\rightarrow I$).[54] These couplings rely on the imaginary part of the off-diagonal terms of the electronic Hamiltonian, and can be understood as higher order effects in comparison with TDCs. The inclusion of these effects is beyond the scope of the present model. As described below, we approximate $E_{\mathrm{res}}(\mathbf{R})$ by anion state energies obtained from quantum chemical calculations (apart from model corrections), and the non-adiabatic couplings are calculated in a similar fashion.

We employ the semilocal approximation[29,66] which keeps the energy dependence of the entry widths, as indicated in eqn (1), along with the local approximation for the complex potentials that govern the time propagation. In doing so, we impose a decomposition of the entry width,

$$\Gamma(\mathbf{R},E) = g^2(\mathbf{R})\gamma(E), \tag{2}$$

where the purely geometry dependent factor $g(\mathbf{R})$ is unitless. This procedure avoids ill behaved cross sections for near-threshold collisions, with no significant increase in the numerical effort to propagate the nuclear wave packets.[66] It is also convenient to employ the model form

$$\Gamma(\mathbf{R}, E) = \Gamma_{\mathrm{L}}(\mathbf{R})\frac{\gamma(E)}{\gamma(E_{\mathrm{res}}(\mathbf{R}))}, \tag{3}$$

which ensures that $\Gamma(R,E_{\mathrm{res}}(\mathbf{R})) = \Gamma_{\mathrm{L}}(R)$ for on-resonance collisions, consistent with the definition of the local-approximation resonance energy as a pole of the K-matrix.[29] The energy dependence is modeled as

$$\gamma(E) = E^{l+1/2}\exp(-bE), \tag{4}$$

according to Berman *et al.*,[67] such that choosing the parameter l as the lowest symmetry-allowed partial wave component recovers the Wigner thresold law.[68] Based on electron scattering calculations, we propose analytical models for the $\gamma(E)$ and $\Gamma_{\mathrm{L}}(\mathbf{R})$ functions (details and numerical procedures discussed in Section 2.2). In addition, the broadening function in eqn (1) is assumed to have a Lorentzian form as in previous studies,[53,54]

$$f_\lambda(\mathbf{R}_0, E) = \frac{1}{\pi}\frac{\lambda/2}{(E - E_{\mathrm{res}}(\mathbf{R}_0))^2 + (\lambda/2)^2}, \tag{5}$$

which is normalized for any value of the phenomenological width λ and energy E_{res}.

2.1 The survival probabilities

The term $\wp_j$ in eqn (1) accounts for the autoionization probability along the dynamics, and it is dependent on the particular fragmentation channel of interest in σ_{DEA}. It is written as

$$\mathcal{P}_j = \sum_{n_j=1}^{N^j_{\mathrm{TBF}}} \theta^{n_j}_{\mathrm{DEA}} P^{n_j}_{\mathrm{sv}}(t \rightarrow \infty), \tag{6}$$

where N^j_{TBF} is the total number of TBFs arising from the j-th initial condition along the dynamics, the index n_j runs over that set of TBFs and $t \rightarrow \infty$ is in practice taken as the final simulation time, t_{final}. The factor $\theta^{n_j}_{\mathrm{DEA}}$ equals one if the TBF undergoes the fragmentation process of interest and zero otherwise. The sum over n_j in eqn (6) is therefore restricted to the TBFs that contribute to the dissociation reaction under consideration.

The final survival probability, $P_{\mathrm{sv}}(t_{\mathrm{final}})$, is a fundamental piece in our model. We explore a simple example to explain how it is constructed. Let us consider the spawning of a given TBF, labelled k and originally on the state I, which is coupled to the state J. After the non-adiabatic transition we end up with the TBF k on state I and another one, say k', on state J ($I \neq J$ hereafter). Following usual AIMS teminology,[56] the spawning mode initiates at $t = t_{\mathrm{entry}}$, ends at $t = t_{\mathrm{exit}}$, and we defined the dwell time (or spawning duration) simply as $t_{\mathrm{exit}} - t_{\mathrm{entry}}$. For simplicity, in this illustration we neglect non-adiabatic couplings involving the continuum, and also the overlap matrices take the form $S_{II} = S_{JJ} = 1$ and $\dot{S}_{II} = \dot{S}_{JJ} = 0$. The two-level time-dependent Schrodinger equation (TDSE) governing the coefficients during the spawning is given by the system

$$\dot{C}^I_k = -iH^{II}_{kk}C^I_k - iH^{\mathrm{IJ}}_{kk'}C^J_{k'} \tag{7}$$

and

$$\dot{C}^J_{k'} = -iH^{JJ}_{k'k'}C^J_{k'} - iH^{JI}_{k'k}C^I_k. \tag{8}$$

We also impose $C^J_{k'}(t_{\mathrm{entry}}) = 0$ and $|C^I_k(t_{\mathrm{entry}})|^2 = |C^I_k(t_{\mathrm{exit}})|^2 + |C^J_{k'}(t_{\mathrm{exit}})|^2$. As usual, the Hamiltonian is the sum of the nuclear kinetic energy and the electronic Hamiltonian, and the off-diagonal elements can be neglected except for $t \in [t_{\mathrm{entry}},t_{\mathrm{exit}}]$.

The inclusion of the discrete-continuum coupling modifies the electronic Hamiltonian, which gains an imaginary part (resonance width). Since we neglect the off diagonal elements of Γ, the modified Hamiltonian relates to the real-valued one (usual AIMS) by $\tilde{H}^{II}_{kk} = H^{II}_{kk} - i\Gamma^I_k/2$ and $\tilde{H}^{JJ}_{k'k'} = H^{JJ}_{k'k'} - i\Gamma^J_{k'}/2$. Also, $\tilde{H}^{IJ}_{kk'} = H^{IJ}_{kk'}$ and $\tilde{H}^{JI}_{k'k} = H^{JI}_{k'k}$, therefore we do not alter the AIMS criteria for entering the spawning mode. The new TDSEs become

$$\dot{\tilde{C}}^I_k = -iH^{II}_{kk}\tilde{C}^I_k - \frac{\Gamma^I_k}{2}\tilde{C}^I_k - iH^{IJ}_{kk'}\tilde{C}^J_{k'} \tag{9}$$

and

$$\dot{\tilde{C}}^J_{k'} = -iH^{JJ}_{k'k'}\tilde{C}^J_{k'} - \frac{\Gamma^J_{k'}}{2}\tilde{C}^J_{k'} - iH^{JI}_{k'k}\tilde{C}^I_k. \tag{10}$$

It is interesting to relate the solutions of eqn (9) and (10) whith those of eqn (7) and (8). Writing the solutions as

$\tilde{C}_k^I(t) = C_k^I(t)f_k(t)$ and $\tilde{C}_{k'}^J(t) = C_{k'}^J(t)f_{k'}(t)$, the f functions for $t < t_{\text{entry}}$ are

$$f_k(t) = f_{k'}(t) = \exp\left[-\frac{1}{2}\int_0^t \Gamma_k^I(t')\mathrm{d}t'\right], \tag{11}$$

while for $t > t_{\text{exit}}$,

$$f_k(t) = \alpha_k \exp\left[-\frac{1}{2}\int_{t_{\text{exit}}}^t \Gamma_k^I(t')\mathrm{d}t'\right] \tag{12}$$

and

$$f_{k'}(t) = \alpha_{k'} \exp\left[-\frac{1}{2}\int_{t_{\text{exit}}}^t \Gamma_{k'}^J(t')\mathrm{d}t'\right], \tag{13}$$

where $\alpha_{k(k')}$ are constants. The exponent in eqn (11) depends only on Γ_k^I, for both electronic states. Even though $C_{k'}^J(t < t_{\text{entry}}) = 0$, the auto-detachment rate of the parent TBF affects the survival probability of the child. That information is passed to the child for $t > t_{\text{exit}}$ such that the $\alpha_{k(k')}$ values ensure the continuity of the f functions. For $t_{\text{entry}} \leq t \leq t_{\text{exit}}$, the solutions are

$$f_{k(k')}(t) = \exp\left[-\frac{1}{2}\int_0^{t_{\text{entry}}} \Gamma_k^I(t')\mathrm{d}t'\right] g_{k(k')}(t_{\text{entry}}, t), \tag{14}$$

where $g_{k(k')}(t_{\text{entry}}, t)$ are continuous functions with initial condition $g_{k(k')}(t_{\text{entry}}, t_{\text{entry}}) = 1$.

The survival probabilities attributed to each TBF depend on the coefficients $\tilde{C}$ at $t = t_{\text{final}} > t_{\text{exit}}$, so ultimately only the solutions 12 and 13 are relevant for the DEA cross sections. In terms of $g_{k(k')}$,

$$\begin{aligned} f_k(t > t_{\text{exit}}) \;=\; & \exp\left[-\frac{1}{2}\int_0^{t_{\text{entry}}} \Gamma_k^I(t')\mathrm{d}t'\right] \\ & \times g_k(t_{\text{entry}}, t_{\text{exit}}) \exp\left[-\frac{1}{2}\int_{t_{\text{exit}}}^t \Gamma_k^I(t')\mathrm{d}t'\right] \end{aligned} \tag{15}$$

and

$$\begin{aligned} f_{k'}(t > t_{\text{exit}}) \;=\; & \exp\left[-\frac{1}{2}\int_0^{t_{\text{entry}}} \Gamma_k^I(t')\mathrm{d}t'\right] \\ & \times g_{k'}(t_{\text{entry}}, t_{\text{exit}}) \exp\left[-\frac{1}{2}\int_{t_{\text{exit}}}^t \Gamma_{k'}^J(t')\mathrm{d}t'\right]. \end{aligned} \tag{16}$$

Finally, we make another approximation on expressions (15) and (16). We approximate

$$f_k(t > t_{\text{exit}}) \approx \exp\left[-\frac{1}{2}\int_0^t \Gamma_k^I(t')\mathrm{d}t'\right] \tag{17}$$

for the parent TBF, and

$$f_{k'}(t > t_{\text{exit}}) \approx \exp\left[-\frac{1}{2}\int_0^{t_{\text{entry}}} \Gamma_k^I(t')\mathrm{d}t' - \frac{1}{2}\int_{t_{\text{entry}}}^t \Gamma_{k'}^J(t')\mathrm{d}t'\right] \tag{18}$$

for the child, in such a way that the survival probability P_{sv} of the two TBFs considered in this example can be written as

$$P_{\text{sv}}^k(t_{final}) \approx p_k \exp\left[-\int_0^{t_{final}} \Gamma_k^I(t')dt'\right] \tag{19}$$

and

$$P_{\text{sv}}^{k'}(t_{\text{final}}) \approx p_{k'} \exp\left[-\int_{t_0}^{t_{\text{entry}}} \Gamma_k^I(t')\mathrm{d}t' - \int_{t_{\text{entry}}}^{t_{\text{final}}} \Gamma_{k'}^J(t')\mathrm{d}t'\right], \tag{20}$$

where $p_k = |C_k^I(t_{\text{final}})|^2$ and $p_{k'} = |C_{k'}^J(t_{\text{final}})|^2$ are the AIMS populations of the TBFs on state I and J at the final simulation time. This approximation is the same of making

$$g_k(t_{\text{entry}}, t_{\text{exit}}) \approx \exp\left[-\frac{1}{2}\int_{t_{\text{entry}}}^{t_{\text{exit}}} \Gamma_k^I(t')\mathrm{d}t'\right] \tag{21}$$

and

$$g_{k'}(t_{\text{entry}}, t_{\text{exit}}) \approx \exp\left[-\frac{1}{2}\int_{t_{\text{entry}}}^{t_{\text{exit}}} \Gamma_{k'}^J(t')\mathrm{d}t'\right], \tag{22}$$

which clearly becomes accurate when the dwell time is short. In AIMS simulations, $t_{\text{exit}} - t_{\text{entry}}$ is often on the order of a few femtoseconds.

In practical cases, one initial condition may give rise to several child TBFs, and the concept can be easily generalized as illustrated in Fig. 2.

2.2 Complex potential models

We performed fixed-nuclei elastic electron scattering simulations to obtain accurate estimates for the positions and widths of the π_1^*, σ_{CBr}^* and π_2^* anion states. Eigenphase sums and integral cross sections (ICSs) were computed with the Schwinger Multichannel (SMC) method[69,70] implemented with the norm-conserving pseudopotentials proposed by Bachelet, Hamann and Schluter.[71,72] The details of the method are described elsewhere,[73] and since we proceed along the lines of the previous scattering calculations for BrU,[41] the numerical procedures are given as ESI.†

For neutral BrU, the lowest energy geometry of the ground state is planar, so the eigenphase sum and the ICS can be decomposed into the A' and A'' components of the C_s group. At the minimum of the neutral molecule PES, π_1^* is a valence bound state, while σ_{CBr}^* and π_2^* are shape resonances with A' and A'' symmetry, respectively. As discussed below, the scattering results are used to build the complex potential models employed in the AIMS-based DEA dynamics. Since we pay special attention to the dissociation coordinate, the cross sections and eigenphases were computed for different C_5–Br bond lengths, described as displacements, $\Delta R_{\text{CBr}} = (R_{\text{CBr}} - R_{\text{CBr}}^{\text{eq}}) = -0.2$ Å, -0.1 Å, 0, +0.1 Å and +0.2 Å, where $R_{\text{CBr}}^{\text{eq}}$ is the equilibrium bond length. Since the remaining geometric parameters were kept fixed, the A'/A'' decomposition could be performed in all cases.

The symmetry-resolved ICS is shown in Fig. 3a (A') and b (A''). As expected, the energies and widths of the π_2^* anion states do not strongly depend on the C_5–Br bond length, in contrast to the σ_{CBr}^* resonance, and the results obtained for the equilibrium geometry are in good agreement with the electron transmission[74] and DEA[75] data.

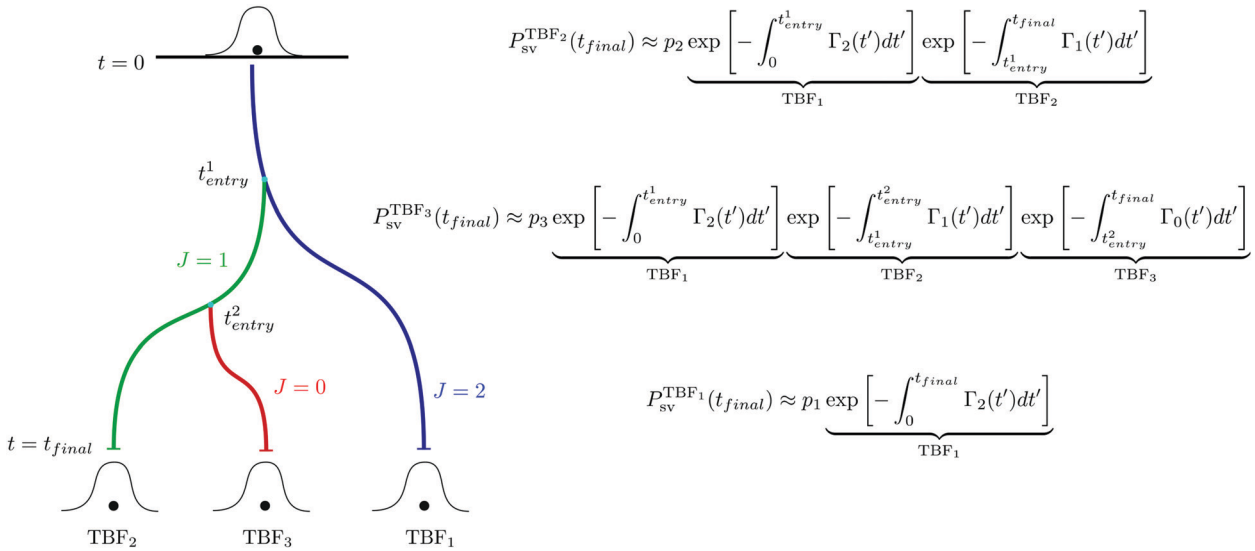

Fig. 2 Scheme illustrating how the survival probabilities are evaluated in practical simulations. In this example, at t = 0 the simulation is initiated with one single TBF, representing the initial condition, and it terminates at $t = t_{\mathrm{final}}$ with TBFs 1, 2 and 3, with final populations p_1, p_2 and p_3. The concept used to build equation? is replicated as many times as the number of spawnings, and the P_{sv}'s are calculated as shown on the right. The times $t_{\mathrm{entry}}{}^1$ and $t_{\mathrm{entry}}{}^2$ denote t_{entry} for spawnings 1 and 2, respectively.

From the corresponding eigenphase sums (δ_{sum}), we obtained the positions (E_{res}) and widths (Γ_{L}) of the shape resonances by performing least-squares fits of the standard local-approximation formula,

$$\delta_{\mathrm{sum}}(E,\mathbf{R}) = -\arctan\left(\frac{\Gamma_L(\mathbf{R})/2}{E - E_{\mathrm{res}}(\mathbf{R})}\right) + \delta_{\mathrm{bg}}(E,\mathbf{R}), \qquad (23)$$

to the eigenphase sums computed with the SMC method. The dependence on the nuclear coordinates is indicated in the above expression, where $\delta_{\mathrm{bg}}(E)$ is the background component, which was modelled with a second degree polynomial.

The definition of a resonance state as pole of the K-matrix,[29] establishes a relation between the local position and width, $\Gamma_{\mathrm{L}}(R) = \Gamma(R,E_{\mathrm{res}}(\mathbf{R}))$, which is useful to build complex potential models.[53,54,76] For the π^*_2 shape resonance, the linear relation

$$\Gamma^{\pi^*_2}_{\mathrm{L}}(\mathbf{R}) = 0.0471 E^{\pi^*_2}_{\mathrm{res}}(\mathbf{R})[\mathrm{eV}] \qquad (24)$$

provided a good description of the weak geometry dependence, as shown in Fig. 3c. It should be clear that the Wigner threshold law is relevant for the entry width, given in eqn (4), but not for the local width, Γ_{L}, used to compute the autoionization survival probability.[66] For the σ^*_{CBr} shape resonance, we employed the form $\Gamma_{\mathrm{L}} = E^{\alpha}\exp(-\beta E)$, based on previous studies,[66,76] obtaining

$$\Gamma^{\sigma^*_{\mathrm{CBr}}}_{\mathrm{L}}(\mathbf{R}) = [E^{\sigma^*_{\mathrm{CBr}}}_{\mathrm{res}}(\mathbf{R})]^{0.892} \exp\left(-0.228 E^{\sigma^*_{\mathrm{CBr}}}_{\mathrm{res}}(\mathbf{R})\right)[\mathrm{eV}]. \qquad (25)$$

The σ^*_{CBr} state stabilizes as the C_5Br bond stretches, becoming a bound state for ΔR_{CBr} = 0.1 Å and 0.2 Å, such that we only used three points to obtain eqn (25), namely ΔR_{CBr} = −0.2 Å, −0.1 Å and the equilibrium bond length. In addition, the large background in the A' symmetry component, arising from the dipolar interaction,[41] increases the uncertainties of the resonance parameters, *i.e.*, the background makes the eigenphase model in eqn (23) more difficult. Both the small number of points underlying eqn (25), and the spread of those points arising from the large background, would be expected to affect

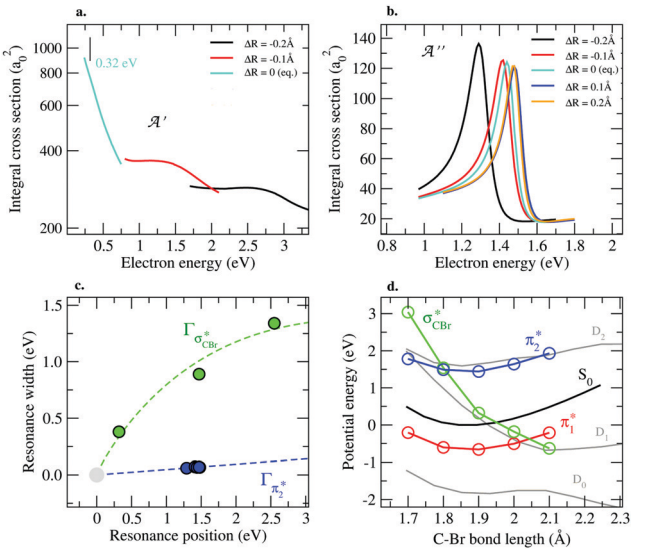

Fig. 3 (Upper panels) Integral cross sections for different geometries of BrU decomposed in A' (upper left) and A'' (upper right) components, as functions of the incident electron energy (in eV). The colors black, red, cyan, blue and orange represent ΔR_{CBr} = −0.2 Å, −0.1 Å, 0 (optimized geometry), +0.1 Å and +0.2 Å, respectively. The blue and orange curves are omitted from the A' plot because the σ^*_{CBr} anions are bound states at those geometries. (Lower left) Resonance widths (in eV) for both σ^*_{CBr} and π^*_2 anions as functions of the resonance positions (in eV). The green and blue dashed lines represent the polynomial fit. (Lower right) Real part of the potential energy curves of the neutral ground state (S_0) and the three studied anions. The solid grey lines indicate the adiabatic FOMO-CASCI doublets.

the quality of our results. Fortunately, the non-adiabatic transtions typically take place in early times of the dynamics, essentially within the Franck–Condon region of the neutral molecule, making the calculated DEA cross section rather insensitive to the $\Gamma_{\mathrm{L}}^{\sigma^*_{\mathrm{CBr}}}$ model (see below). In fact, we performed simulations with a different model, employing a third-order polynomial instead of eqn (25). As shown in the ESI,† the polynomial model provides a better fit (smaller variance), although with unphysical oscillations. The DEA cross section obtained with both models are similar, demonstrating that the dynamics is only sensitive to the resonance states in the vicinity of the equilibrium geometry of the neutral BrU molecule. Most of the dynamics takes place on the bound anion ground state, where $\Gamma_{\mathrm{L}} = 0$.

We also need to estimate the parameter b in eqn (4), related to the energy dependence of the semilocal entry width, eqn (3). Since our model assumes electron attachment to the π_2^* shape resonance, we also imposed $l = 1$ in eqn (4), according to the Wigner Law (the p-wave is lowest symmetry-allowed partial wave in the A'' component). The parameter was estimated from the least-squares fit of a non-local model to the eigenphase sum computed with the SMC method at the optimal geometry of the neutral molecule, R_0. The model is given by

$$\delta_{\mathrm{sum}}(E,\mathbf{R}_0) = -\arctan\left(\frac{g^2(\mathbf{R}_0)\gamma(E)/2}{E-\varepsilon_{\mathrm{d}}-\Delta_S(E,\mathbf{R}_0)}\right) + \delta_{\mathrm{bg}}(E,\mathbf{R}_0), \quad (26)$$

and

$$\Delta_S(E,\mathbf{R}_0) = \frac{1}{2\pi}\mathscr{P}\int \mathrm{d}E' \frac{\Gamma(E',\mathbf{R}_0)}{E-E'} = \frac{g^2(\mathbf{R}_0)}{2\pi}\mathscr{P}\int \mathrm{d}E' \frac{\gamma(E')}{E-E'}, \quad (27)$$

where $\mathscr{P}$ indicates the Cauchy's principal value. Using well-known formulas[67] for the real level-shift Δ_S, and a second degree polynomial for the background, we obtained b = 0.44 eV^{-1}. Once more, we carried out exploratory studies to assess the robustness of the model, and we find the DEA cross sections to be little affected by parameter values within $0 \leq b \leq$ 1.0 eV. The explanation for the weak dependence on b mostly relies on the influence of the parameter on the semilocal entry width for energies near E_{res}, where $\gamma(E)/\gamma(E_{\mathrm{res}}(\mathbf{R})) \sim 1$ independently of b. It is worth noting that the broadening function (5) makes the contributions from energies around the resonance position more important.

2.3 Computational details and numerical procedures

The AIMS simulations require energies, gradients and couplings at every time step, so caution must be taken to keep the numerical effort at a reasonable level. The real part of the TNI complex potentials were approximated by anion states obtained with the fractional occupancy molecular orbital – complete active space – configuration interaction (FOMO-CASCI) method.[77] We employed the 6-31+G(d) basis set and a small active space comprising 3 electrons in 4 orbitals, performing the electronic structure calculations with the GPU-accelerated version of TeraChem software.[78–80] The reference for the CASCI is the electronic structure of the neutral BrU, and the 4 orbitals included in the active space are the HOMO (π_1), LUMO(π_1^*), LUMO + 1$(\sigma^*_{\mathrm{CBr}})$ and LUMO + 2(π_2^*), where the last three are displayed on Fig. 1. The broadening parameter β was fixed at 0.2 a.u. Since the neutral species is a closed shell molecule, the anion states are doublets indicated as D_J, with J = 0, 1, 2. At the vertical attachment geometry, these states correspond to the valence bound π_1^* state, and the σ^*_{CBr} and π_2^* shape resonances, in order of increasing energy. The dipole bound state (DBS)[41] was not included in the dynamics. The compact basis set and active space employed in our model are suitable to reduce the computational effort, and they also give rise to anion states with clearly defined electronic character, avoiding significant admixtures of pseudo-continuum states. The description of the DBS would require an agmented active space and very diffuse basis sets that could give rise to numerical instabilities. We only consider initial conditions on the π_2^* potential surface, which is expected to couple more strongly to the closer-lying σ^*_{CBr} resonance than to the DBS. While the DBS could play a role in the DEA dynamics, in view of the expected couplings to the π_1^* and σ^*_{CBr} anion states, we presently explore the model described above, postponing the inclusion of DBSs in mixed quantum-classical DEA simulations to future work.

The D_1 and D_2 anion states are obtained along the AIMS dynamics as the anion ground state, D_0. The excitation energies should be rescaled to represent anion energies with respect to the ground state of the neutral species, so the resonance energies are formally expressed as

$$E^J_{\mathrm{res}}(\mathbf{R}) = \varepsilon_J(\mathbf{R}) - \Delta(\mathbf{R}), \quad (28)$$

where $\varepsilon_J = (E_{\mathrm{D}_J} - E_{\mathrm{D}_0})$ is the excitation energy of the J-th anion state with respect to the D_0 bound state, presently obtained with the FOMO-CASCI method, and $\Delta = (E_{\mathrm{S}_0} - E_{\mathrm{D}_0})$ is the binding energy of the anion with respect to neutral ground state, S_0. In practice, $\Delta(\mathbf{R})$ is an empirical correction to enforce accurate resonance energies, which is only relevant for the TNI dynamics, not for the D_0 bound state (see below). For most of the initial conditions, we verified that the decays to D_0 take place within the Franck–Condon (FC) region of S_0, so we only need to compute $\Delta(\mathbf{R})$ for small distortions with respect to the S_0 minimum, $\mathbf{R}_0$. We therefore employed the simple approximation $\Delta(\mathbf{R}) = \Delta_0(\mathbf{R}) + \delta$, where $\Delta_0(\mathbf{R})$ is the binding energy computed with the FOMO-CASCI and Hartree–Fock (HF) energies for D_0 and S_0, respectively, while δ is a constant shift to tune the vertical resonance energies from eqn (28) to those obtained with scattering calculations at the optimal geometry of the neutral molecule.

The potential energy curves along the C_5–Br coordinate are shown in Fig. 3d. In those geometries, the doublets D_0, D_1 and D_2 correspond to the π_1^*, σ^*_{CBr} and π_2^* anions. The vertical shift δ = 5.34 eV was chosen to impose the agreement between the position of the π_2^*, obtained from the SMC method, and the energy of the D_2 FOMO-CASCI state at the equilibrium geometry of the neutral ground state. This same vertical shift was

reasonable for the other bond lengths, and also for the σ^*_{CBr} resonance and the D_1 state. We therefore employed the same constant shift for both resonances at all relevant geometries, *i.e.*, prior to the decay to the D_0 state along the dynamics. It is worth emphasizing that we perform standard AIMS simulations for the anion states, relying on the FOMO-CASCI wave functions and non-adiabatic couplings described above, so the complex potential models given in eqn (24), (25) and (28) are only used to compute the survival probabilities in eqn (1). In addition, further investigations on the quality of FOMO-CASCI description of the states were conducted with a higher level of electronic structure theory. Fig. S1 of the ESI,† shows the comparison between the potential energy curves, along the R_{CBr} reaction coordinate, of the doublet states with those obtained with the multistate CASPT2 level of theory. Although the curves present similar features up to $R_{CBr} \sim 2.3$ Å, the main differences rely on the topology of D_1 state and the geometry in which $E_{D_1} - E_{D_0}$ is minimized, about 0.1 Å lower than the FOMO-CASCI prediction. Another difference is the energy barrier along D_0 associated with this transition state, which is about 0.2 eV lower at the FOMO-CASCI level. The comparison between the levels of theory suggests that the FOMO-CASCI may favor the Br^- dissociation, when compared with the CASPT2, although a rigorous analysis requires entire simulations with different electronic strucuture levels.

In the present work, the criteria for AIMS to enter the spawning region was based on the projection of the non-adiabatic coupling vector, $\mathbf{d}_{IJ}$, on the classical velocities of the TBFs, $\Lambda^{\text{eff}}_{IJ}(\mathbf{R}) = |\mathbf{d}_{IJ}(\mathbf{R})\cdot\mathbf{R}|$, with the numerical threshold 0.02 a.u.

2.4 Nuclear ensemble and temperature effects

Gas-phase DEA measurements for BrU and other halouracils were reported for temperatures around 420 K to 470 K.[49–51] While we performed room-temperature simulations, temperature effects were investigated with the importance sampling of the nuclear ensemble initial conditions.[81] We start from a standard Wigner sampling[82] at T_0 = 300 K, computing the DEA cross section with eqn (1). For different temperatures, the weight of the j-th initial condition is rescaled with

$$w(\mathbf{R}_0^j, \mathbf{P}_0^j) = \prod_{i=1}^{3N_{\text{atom}}-6} \frac{\alpha_i^T}{\alpha_i^{T_0}} \exp\left[-\left(\alpha_i^T - \alpha_i^{T_0}\right)\left(\frac{\mu_i\omega_i(R_0 i^j)^2}{\hbar} + \frac{(P_0 i^j)^2}{\mu_i\omega_i\hbar}\right)\right], \quad (29)$$

where $\alpha_i^T = \tanh(\hbar\omega_i/2k_BT)$, R_{0i}^j is the initial value for the i-th normal coordinate of the neutral target, P_{0i}^j the corresponding momentum, μ_i is the reduced mass, and ω_i the angular frequency. The w factors in eqn (29) correct the Wigner weights generated for T_0 = 300 K to those for $T \neq T_0$.

3 Results and discussion

We obtained 122 trajectories from 21 initial conditions, thus generating ≈6 TBFs per initial condition. Fig. 4a–c show superpositions of all the initial and spawning geometries for the D_2/D_1 and D_1/D_0 transitions. The plots indicate modest geometry distortion suggesting that internal conversion takes place around the FC region of the neutral molecule. The spawning times are shown in the histogram plots, pointing out that 66% of D_2/D_1 conversions occur in less than 50 fs, while the D_1/D_0 transition frequency reaches a maximum around 50 fs and then decreases monotonically. The distribution of spawning times in Fig. 4a and b was obtained from the AIMS dynamics without accounting for autoionization. The survival probability on the π_2^* resonance, corresponding to the D_2 state in early times of the dynamics, is below 1% for t = 50 fs, such that all the D_2/D_1 transitions relevant to DEA occur in the first few tens of femtoseconds.

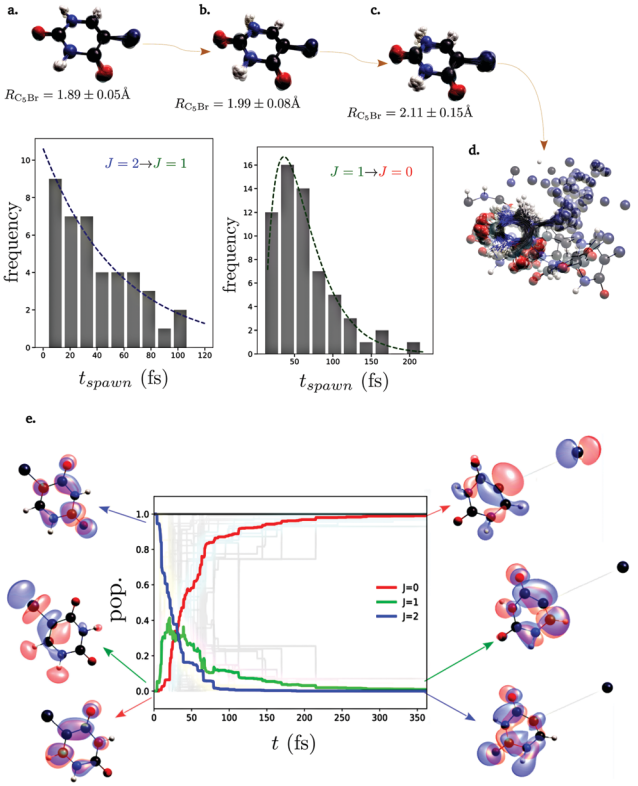

Fig. 4 Superposition of all (a) initial geometries, (b) $J = 2 \rightarrow J = 1$ spawning geometries, (c) $J = 1 \rightarrow J = 0$ spawning geometries and (d) final geometries. Distributions of spawning times t_{spawn} are presented in the two histograms, referring to (b) and (c) decay processes. Mean values of the coordinate R_{C_5Br} for the (a), (b) and (c) sets are also indicated. (e) Population $P_J(t)$ of the electronic states J = 0, 1, 2 obtained over 122 TBFs. The thinner grey lines represent each initial condition. On the panel sides it is shown the nature of all electronic states (SOMOs) at the beginning and at the end of the simulation.

The AIMS population dynamics, also neglecting autoionization, is shown in Fig. 4(e). The thin gray lines correspond to different trajectories while the thick lines indicate the average populations, $P_J(t)$, for J = 0 (red), J = 1 (green) and J = 2 (blue). The population is initially transferred from D_2 to D_1, although significant probability is observed in the D_0 state in early simulation times, around 25 fs. The population of the J = 1 state reaches a maximum around 30 fs, while the ground state population increases monotonically, reaching 0.6 around 50 fs.

From exponential fits, we obtained the time constant 38.7 fs for the decay of the D_2 state, and 56.8 fs for the probability transfer to the D_0 state. In summary, the results in Fig. 4 indicate that the non-adiabatic decay from D_2 to the anion ground state takes place in the first $\approx$50 fs of the dynamics. This fast decay is of course relevant to the DEA reactions that compete with the autoionization channels.

The non-adiabatic dynamics also points out different dissociation mechanisms. The anion molecule may undergo dissociation through the cascade $\pi_2^*(D_2) \rightarrow \sigma_{CBr}^*(D_1) \rightarrow \sigma_{CBr}^*(D_0)$, or it may form a vibrationally hot $\pi_1^*(D_0)$ state, which dissociates stochastically. All TBFs will therefore undergo some fragmentation if the trajectories are propagated for long enough. Out of the final 122 TBFs, 76 dissociated into $Uyl^{\bullet} + Br^-$ for t_{final} = 380 fs.

The time evolution of relevant parameters are shown in Fig. 5. Specifically, we consider the C_5–Br (R_{C_5Br}) and N_1–H (R_{N_1H}) bond lengths, the ring puckering angle (φ) and the angle (ϕ_{C_5}) describing the out-of-plane motion of the bromine atom. The thin gray lines correspond to the TBFs, while the thick lines indicate averages for the anion states J = 0 (red), J = 1 (green) and J = 2 (blue). The average R_{C_5Br} bond length of the anion ground state increases somewhat slowly as a function of time. The gray lines also suggest that halide elimination does not arise immediately after the decay to D_0 state, but rather over a long span of time (10^2 fs). The symmetry-breaking coordinates

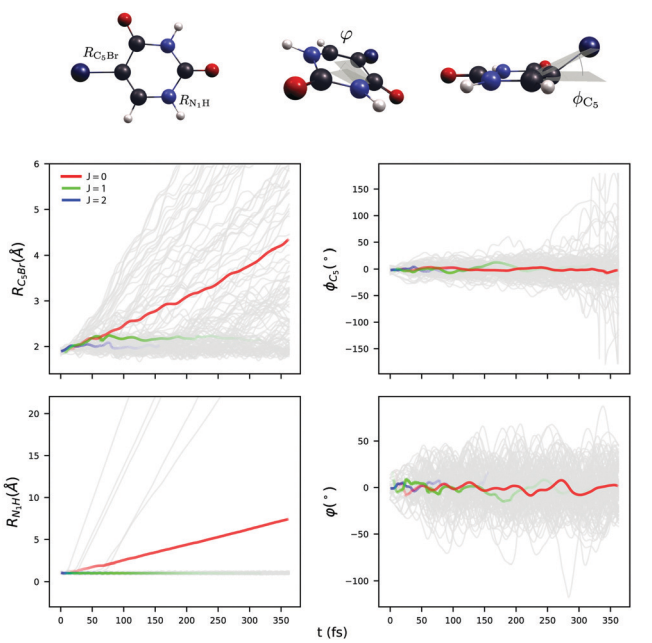

Fig. 5 Time evolution of internal coordinates of anion BrU along the AIMS simulation. The left two panels show the time evolution of the reactive coordinates R_{C_5Br} and R_{N_1H}, while the right two panels show the evolution of internal angles ϕ_{C_5} and φ which lead to nonplanarity (coordinates schematically displayed in the upper part of the figure). Thin grey lines represent distinct TBFs while the colored thicker lines represent averages for each J. The opacities of the colored lines are proportional to the population.

φ and ϕ_{C_5} should also play a role in the DEA dynamics because the π_2^*/σ_{CBr}^* coupling would be forbidden by symmetry if the planarity was preserved. As seen in Fig. 5, the average of the ϕ_{C_5} coordinate for the J = 0 state does not significantly deviate from zero. On the other hand, the average values of the φ coordinate, defined as C_2–N_3–C_4–C_5 torsion angle, show significant oscillations, around -20° and 20°, in the three anion states.

The AIMS simulations also point to hydrogen elimination from the N_1–H bond as a possible DEA channel, as inferred from the dynamics of the R_{N_1H} coordinate, shown in Fig. 5. However, only 5 trajectories produced that dissociation reaction (see the gray lines). The AIMS population at t_{final} of these five TBFs sum up less than 0.03, indicating a low probability for the reaction. Besides, typically, σ_{NH}^* resonances are very broad,[31] which would cause the corresponding survival probabilities to vanish very quickly. Because of this, and also because H elimination from BrU was not observed in DEA measurements, we excluded the σ_{NH}^* orbital from the active space in our model. Nevertheless, the molecule could access regions of the configuration space where one of the adiabatic electronic states developed σ_{NH}^* character, leading to rare N_1–H bond breaking events. In addition, we have observed ring opening and other complex outcomes in three TBFs of distinct ICs. However, the AIMS populations of these TBFs at t_{final} are less than 0.06, and they will not be discussed further.

The results in Fig. 5 indicate that several trajectories have long dissociation times in comparison to the fixed-nuclei resonances lifetimes. However, the survival probabilities converge to constant values as the anion becomes more stable than the neutral molecule, since in this case Γ_L = 0. The most significant contributions to the DEA cross section arise from the trajectories that undergo fast transitions to the bound anion (Fig. 6 – bottom). Basically every TBF that lives long enough to undergo internal conversion to the D_0 state will dissociate, in view of the significant energy of the initial π_2^* anion state ($\approx$1.4 eV), but the contribution of the TBFs to the DEA cross section is weighted by the survival probabilities, which are larger for the transitions that occur at earlier times. In Fig. 6 we show the distribution of stabilization times, defined as the instant the TBFs decay to D_0. The onset of stabilization is around $\sim$7 fs, and from a biexponential fit (dashed line) we estimate the maximum of the distribution at 18.6 fs. The final survival probabilities, over 122 TBFs, range from 10^{-10} to $\sim 10^{-1}$, which corroborates that fast decays are essential to build up the DEA cross section.

Finally, the DEA cross section was calculated with eqn (1) once all P_{sv} were computed. Fig. 7 presents the results along with the experimental data reported by Abdoul-Carime *et al.*[49] The measurements correspond to the negative ion yield as a function of the incident electron energy, which were not normalized to a cross section. Nevertheless, the authors estimated the cross section peak height as $\sim 10^{-15}$ cm^2 (tens of a_0^2) for Br^- in gas phase BrU. The sensitivity of our model in respect to the parameters δ and λ is presented in Fig. S3 and S4 of the ESI.†

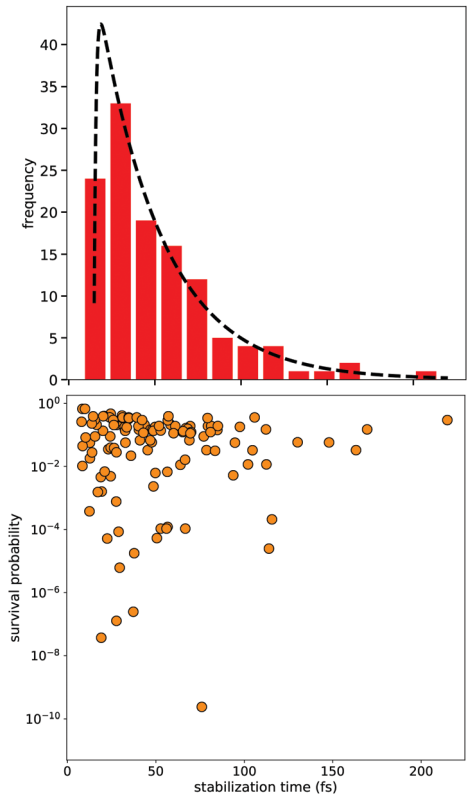

Fig. 6 (Top) Distribution of stabilization times, in fs, obtained from the 122 TBFs. (Bottom) Survival probavilities of all TBFs against their stabilization times, in fs.

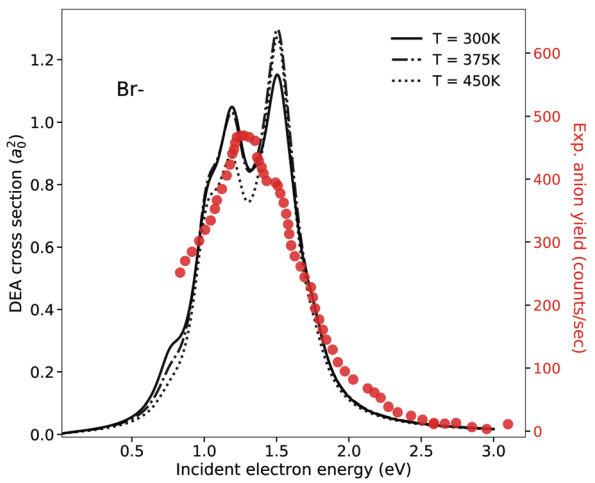

Fig. 7 DEA cross section for Br^- dissociation of BrU obtained within our model using λ = 0.22. The curves for T = 375 K and T = 450 K were obtained with the corrections (29). For comparison, the graphics also show experimental data (red) reported by Abdoul-Carime *et al.*[49]

Our DEA cross section curve has a peak intensity of $\sim 1 a_0^2$ (0.3×10^{-16} cm^2), below the experimental estimates by a factor of 3 to 10. Much of this disagreement may be due to the crudeness of the experimental cross section estimation. However, we would not be surprised that some of this underestimation is due to incompleteness of our model. While the local and semi-local width fittings/parametrizations had no significant impact on the DEA magnitudes, a more accurate treatment of electron correlation could, in princple, impact the spawning and stabilization times (affecting the survival probability), although this is not clearly supported by our CASPT2 calculations (Fig. S1, ESI†). In addition, the fraction of TBFs undergoing C–Br bond breaks might be underestimated. Nonetheless, considering all TBFs – not only those that dissociate – in the calculations increases the peak intensity by 50%.

Lastly, we considered three sample temperatures. No significant differences among the DEA cross sections peak positions and intensities were found. This supports the argument that DEA experiments at 450 K could be, in principle, a good guide to DEA processes at standard thermodynamic conditions, at least for BrU and similar molecules.

Our results indicate Br^- dissociation upon electron attachment, in agreement with experimental observations that Br^- is the most abundant fragment at 1.4 eV. However, minor fragments, namely Uyl^-, $(H_2C_3NO)^-$ and $(OCN)^-$, were also detected experimentally. We did not observe any of these minor products in our simulations. This is likely a consequence of insufficient statistics, as the yield of these minor products in experiments was at least ten times lower than that of Br^-. This could be investigated in future work.

4 Conclusions

We presented a novel theoretical approach for the non-adiabatic dynamics of TNIs based on full-dimensionality complex-valued potential energy surfaces. As a first case we conducted a study of the dissociative electron attachment to BrU. We consider the low-energy electron attachment to the π_2^* resonance of BrU and the subsequent formation of the Br^- anion, which in turn is mediated by a π_2^*/σ_{CBr}^* coupling. The propagation of the nuclear wave packet was carried out with AIMS, while the auto-ionization width was modeled with scattering calculations. We also proposed a model to obtain the survival probabilities within the AIMS framework.

Conflicts of interest

There are no conflicts to declare.

Acknowledgements

L. M. C. acknowledges financial support from São Paulo Research Foundation (FAPESP), under grants No. 2015/17273-5 and No. 2018/02257-2, and HPC-USP. M. T. do N. V. acknowledges financial support from Brazilian National Council for Scientific and Technological Development (CNPq), under grant No. 304571/2018-0. This work was partially supported by the AMOS program of the U.S. Department of Energy.

References

1 I. I. Fabrikant, S. Eden, N. J. Mason and J. Fedor, *Advances in atomic, molecular, and optical physics*, Elsevier, 2017, vol. 66, pp. 545–657.

2 L. Bárdos and H. Baránková, *Thin Solid Films*, 2010, **518**, 6705–6713.

3 L. G. Christophorou and J. K. Olthoff, *Fundamental electron interactions with plasma processing gases*, Springer Science & Business Media, 2012.

4 V. Mukundan and A. Bhardwaj, *Astrophys. J.*, 2018, **856**, 168.

5 P. Cicman, J. Skalny, J. Fedor, N. Mason, P. Scheier, E. Illenberger and T. Märk, *Int. J. Mass Spectrom.*, 2007, **260**, 85–87.

6 J. Luo, J. Hu, X. Wei, L. Fu and L. Li, *Chemosphere*, 2015, **131**, 17–33.

7 C. R. Arumainayagam, H.-L. Lee, R. B. Nelson, D. R. Haines and R. P. Gunawardane, *Surf. Sci. Rep.*, 2010, **65**, 1–44.

8 M. Huth, F. Porrati and O. V. Dobrovolskiy, *Microelectron. Eng.*, 2018, **185**, 9–28.

9 R. M. Thorman, R. K. Tp, D. H. Fairbrother and O. Ingólfsson, *Beilstein J. Nanotechnol.*, 2015, **6**, 1904–1926.

10 J. De Teresa, A. Fernández-Pacheco, R. Córdoba, L. Serrano-Ramón, S. Sangiao and M. R. Ibarra, *J. Phys. D: Appl. Phys.*, 2016, **49**, 243003.

11 I. Gonzalez-Martinez, A. Bachmatiuk, V. Bezugly, J. Kunstmann, T. Gemming, Z. Liu, G. Cuniberti and M. Rümmeli, *Nanoscale*, 2016, **8**, 11340–11362.

12 N. J. Mason, B. Nair, S. Jheeta and E. Szymańska, *Faraday Discuss.*, 2014, **168**, 235–247.

13 M. C. Boyer, N. Rivas, A. A. Tran, C. A. Verish and C. R. Arumainayagam, *Surf. Sci.*, 2016, **652**, 26–32.

14 C. R. Arumainayagam, R. T. Garrod, M. C. Boyer, A. K. Hay, S. T. Bao, J. S. Campbell, J. Wang, C. M. Nowak, M. R. Arumainayagam and P. J. Hodge, *Chem. Soc. Rev.*, 2019, **48**, 2293–2314.

15 J. Gu, J. Leszczynski and H. F. Schaefer, *Chem. Rev.*, 2012, **112**, 5603.

16 E. Alizadeh and L. Sanche, *Chem. Rev.*, 2012, **112**, 5578–5602.

17 E. Alizadeh, T. M. Orlando and L. Sanche, *Annu. Rev. Phys. Chem.*, 2015, **66**, 379–398.

18 J. Kohanoff, M. McAllister, G. A. Tribello and B. Gu, *J. Phys.: Condens. Matter*, 2017, **29**, 383001.

19 X. Ren, E. Wang, A. D. Skitnevskaya, A. B. Trofimov, K. Gokhberg and A. Dorn, *Nat. Phys.*, 2018, **14**, 1062–1066.

20 J. Ma, F. Wang, S. A. Denisov, A. Adhikary and M. Mostafavi, *Sci. Adv.*, 2017, **3**, e1701669.

21 J. Ma, A. Kumar, Y. Muroya, S. Yamashita, T. Sakurai, S. A. Denisov, M. D. Sevilla, A. Adhikary, S. Seki and M. Mostafavi, *Nat. Commun.*, 2019, **10**, 1–7.

22 J. Rackwitz, J. Kopyra, I. Dabkowska, K. Ebel, M. L. Ranković, A. R. Milosavljević and I. Bald, *Angew. Chem.*, 2016, **128**, 10404–10408.

23 M. Rezaee, R. P. Hill and D. A. Jaffray, *Radiat. Res.*, 2017, **188**, 123–143.

24 R. Schürmann, T. Tsering, K. Tanzer, S. Denifl, S. Kumar and I. Bald, *Angew. Chem., Int. Ed.*, 2017, **56**, 10952–10955.

25 R. Schürmann, S. Vogel, K. Ebel and I. Bald, *Chem. – Eur. J.*, 2018, **24**, 10271–10279.

26 R. Meißner, J. Kočišek, L. Feketeová, J. Fedor, M. Fárnk, P. Limão-Vieira, E. Illenberger and S. Denifl, *Nat. Commun.*, 2019, **10**, 1–7.

27 J. D. Gorfinkiel, M. T. D. N. Varella and R. Čurík, *et al.*, *Low-Energy Electrons: Fundamentals and Applications*, 2019, **121**.

28 T. C. Jagau, K. B. Bravaya and A. I. Krylov, *Annu. Rev. Phys. Chem.*, 2017, **68**, 525–553.

29 W. Domcke, *Phys. Rep.*, 1991, **208**, 97.

30 J. Fedor, C. Winstead, V. McKoy, M. Čížek, K. Houfek, P. Kolorenč and J. Horáček, *Phys. Rev. A: At., Mol., Opt. Phys.*, 2010, **81**, 042702.

31 G. A. Gallup and I. I. Fabrikant, *Phys. Rev. A: At., Mol., Opt. Phys.*, 2011, **83**, 1–7.

32 I. I. Fabrikant, *Phys. Rev. A*, 2016, **94**, 052707.

33 M. Zawadzki, M. Čížek, K. Houfek, R. Čurík, M. Ferus, S. Civiš, J. Kočišek and J. Fedor, *Phys. Rev. Lett.*, 2018, **121**, 143402.

34 D. J. Haxton, C. W. McCurdy and T. N. Rescigno, *Phys. Rev. A: At., Mol., Opt. Phys.*, 2007, **75**, 012710.

35 D. J. Haxton, T. N. Rescigno and C. W. McCurdy, *Phys. Rev. A: At., Mol., Opt. Phys.*, 2007, **75**, 012711.

36 S. Chourou and A. Orel, *Phys. Rev. A: At., Mol., Opt. Phys.*, 2009, **80**, 032709.

37 M. Tarana, K. Houfek, J. Horáček and I. I. Fabrikant, *Phys. Rev. A: At., Mol., Opt. Phys.*, 2011, **84**, 052717.

38 A. Moradmand, D. Slaughter, D. Haxton, T. Rescigno, C. McCurdy, T. Weber, S. Matsika, A. Landers, A. Belkacem and M. Fogle, *Phys. Rev. A: At., Mol., Opt. Phys.*, 2013, **88**, 032703.

39 C. H. Yuen, N. Douguet, S. Fonseca dos Santos, A. E. Orel and V. Kokoouline, *Phys. Rev. A*, 2019, **99**, 032701.

40 D. S. Slaughter, T. Weber, A. Belkacem, C. S. Trevisan, R. R. Lucchese, C. W. McCurdy and T. N. Rescigno, *Phys. Chem. Chem. Phys.*, 2020, **22**, 13893.

41 F. Kossoski and M. T. D. N. Varella, *Phys. Chem. Chem. Phys.*, 2015, **17**, 17271.

42 F. Kossoski, M. H. F. Bettega and M. T. D. N. Varella, *J. Chem. Phys.*, 2014, **140**, 024317.

43 F. Kossoski and M. T. D. N. Varella, *J. Chem. Phys.*, 2017, **147**, 164310.

44 G. Iliakis, G. Pantelias and S. Kurtzman, *Radiat. Res.*, 1991, **125**, 56.

45 P. Wardman, *Clin. Oncol.*, 2007, **19**, 387.

46 C.-R. Wang and Q.-B. Lu, *J. Am. Chem. Soc.*, 2010, **132**, 14710.

47 Z. Li, P. Cloutier, L. Sanche and J. R. Wagner, *J. Phys. Chem. B*, 2011, **115**, 13668–13673.

48 A. Keller, J. Rackwitz, E. Cauët, J. Liévin, T. Körzdörfer, A. Rotaru, K. V. Gothelf, F. Besenbacher and I. Bald, *Sci. Rep.*, 2014, **4**, 7391.

49 H. Abdoul-Carime, M. A. Huels, F. Brüning, E. Illenberger and L. Sanche, *J. Chem. Phys.*, 2000, **113**, 2517.

50 H. Abdoul-Carime, M. a. Huels, E. Illenberger and L. Sanche, *Int. J. Mass Spectrom.*, 2003, **228**, 703–716.
51 R. Abouaf, J. Pommier and H. Dunet, *Int. J. Mass Spectrom.*, 2003, **226**, 397–403.
52 M. Ben-Nun, J. Quenneville and T. J. Martínez, *J. Phys. Chem. A*, 2000, **104**, 5161–5175.
53 F. Kossoski, M. T. N. Varella and M. Barbatti, *J. Chem. Phys.*, 2019, **151**, 224104.
54 F. Kossoski and M. Barbatti, *Chem. Sci., Adv. Article*, 2020, **118**, 7026–7068.
55 R. Crespo-Otero and M. Barbatti, *Chem. Rev.*, 2018, **118**, 7026–7068.
56 B. F. Curchod and T. J. Martínez, *Chem. Rev.*, 2018, **118**, 3305–3336.
57 L. Lehr and W. H. Miller, *Chem. Phys. Lett.*, 1996, **250**, 515–522.
58 Y. Sugioka and T. Takayanagi, *Chem. Phys.*, 2012, **405**, 189–196.
59 R. Crespo-Otero and M. Barbatti, *Theor. Chem. Acc.*, 2012, **131**, 1237.
60 J. Quenneville, M. Ben-Nun and T. J. Martínez, *J. Photochem. Photobiol., A*, 2001, **144**, 229.
61 T. J. Martínez, *Acc. Chem. Res.*, 2006, **39**, 119.
62 H. R. Hudock, B. G. Levine, A. L. Thompson, H. Satzger, D. Townsend, N. Gador, S. Ullrich, A. Stolow and T. J. Martínez, *J. Phys. Chem. A*, 2007, **111**, 8500.
63 A. M. Virshup, C. Punwong, T. V. Pogorelov, B. A. Lindquist, C. Ko and T. J. MartÌnez, *J. Phys. Chem. B*, 2009, **113**, 3280.
64 A. L. Thompson, C. Punwong and T. J. Martínez, *Chem. Phys.*, 2010, **370**, 70.
65 E. J. Heller, *J. Chem. Phys.*, 1981, **75**, 2923–2931.
66 P. L. Gertitschke and W. Domcke, *Phys. Rev. A: At., Mol., Opt. Phys.*, 1993, **47**, 1031–1044.
67 M. Berman, H. Estrada, L. S. Cederbaum and W. Domcke, *Phys. Rev. A: At., Mol., Opt. Phys.*, 1983, **28**, 1363.
68 E. P. Wigner, *Phys. Rev.*, 1948, **73**, 1002.
69 K. Takatsuka and V. McKoy, *Phys. Rev. A: At., Mol., Opt. Phys.*, 1981, **24**, 2473–2480.
70 K. Takatsuka and V. McKoy, *Phys. Rev. A: At., Mol., Opt. Phys.*, 1984, **30**, 1734–1740.
71 G. B. Bachelet, D. R. Hamann and M. Schluter, *Phys. Rev. B: Condens. Matter Mater. Phys.*, 1982, **26**, 4199.
72 M. H. F. Bettega, L. G. Ferreira and M. A. P. Lima, *Phys. Rev. A: At., Mol., Opt. Phys.*, 1993, **47**, 1111.
73 R. F. da Costa, M. T. D. N. Varella, M. H. F. Bettega and M. A. P. Lima, *Eur. Phys. J. D*, 2015, **69**, 159.
74 A. M. Scheer, K. Aflatooni, G. A. Gallup and P. D. Burrow, *Phys. Rev. Lett.*, 2004, **92**, 3–6.
75 R. Abouaf and H. Dunet, *Eur. Phys. J. D*, 2005, **35**, 405–410.
76 L. M. Cornetta, K. Coutinho and M. T. D. N. Varella, *J. Chem. Phys.*, 2020, **152**, 084301.
77 P. Slavíček and T. J. Martínez, *J. Chem. Phys.*, 2010, **132**, 1.
78 I. S. Ufimtsev and T. J. Martínez, *J. Chem. Theory Comput.*, 2008, **4**, 222.
79 I. S. Ufimtsev and T. J. Martinez, *J. Chem. Theory Comput.*, 2009, **5**, 1004.
80 I. S. Ufimtsev and T. J. Martinez, *J. Chem. Theory Comput.*, 2009, **5**, 2619.
81 F. Kossoski and M. Barbatti, *J. Chem. Theory Comput.*, 2018, **14**(6), 3173–3183.
82 E. Wigner, *Phys. Rev.*, 1932, **40**, 749–759.